Acta Pharmaceutica Sinica B 2024;14(9):4102–4117

Chinese Pharmaceutical Association
Institute of Materia Medica, Chinese Academy of Medical Sciences

Acta Pharmaceutica Sinica B

www.elsevier.com/locate/apsb
www.sciencedirect.com

ORIGINAL ARTICLE

In situ tumor vaccine with optimized nanoadjuvants and lymph node targeting capacity to treat ovarian cancer and metastases

Yuan Li[a,†], Fan Tong[b,†], Yufan Wang[b], Jing Wang[b], Manqi Wu[a], Hanmei Li[c], Hongyan Guo[a,*], Huile Gao[b,*]

[a]*Department of Obstetrics and Gynecology, National Clinical Research Center for Obstetrics and Gynecology, Peking University Third Hospital, Beijing 100191, China*
[b]*Key Laboratory of Drug Targeting and Drug Delivery Systems, West China School of Pharmacy, Sichuan University, Chengdu 610041, China*
[c]*School of Food and Biological Engineering, Chengdu University, Chengdu 610106, China*

Received 22 January 2024; received in revised form 17 April 2024; accepted 20 April 2024

KEY WORDS

In situ nano-vaccine;
Lymph node targeting;
MMP-2 responsive;
PD-1;
Combination therapy;
CpG;
Ovarian cancer;
Metastases

Abstract Tumor vaccine, a promising modality of tumor immunotherapy, needs to go through the process of tumor antigen generation and loading, antigen drainage to lymph nodes (LNs), antigen internalization by dendritic cells (DCs), DC maturation, and antigen cross-presentation to activate T-cells. However, tumor vaccines are often unable to satisfy all the steps, leading to the limitation of their application and efficacy. Herein, based on a smart nanogel system, an *in situ* nano-vaccine (CpG@Man-P/Tra/Gel) targeting LNs was constructed to induce potent anti-tumor immune effects and inhibit the recurrence and metastasis of ovarian cancer. The CpG@Man-P/Tra/Gel exhibited MMP-2-sensitive release of trametinib (Tra) and nano-adjuvant CPG@Man-P, which generated abundant *in situ* depot of whole-cell tumor antigens and formed *in situ* nano-vaccines with CpG@Man-P. Benefiting from mannose (Man) modification, the nano-vaccines targeted to LNs, promoted the uptake of antigens by DCs, further inducing the maturation of DCs and activation of T cells. Moreover, CpG@Man-P with different particle sizes were prepared and the effective size was selected to evaluate the antitumor effect and immune response *in vivo*. Notably, combined with PD-1 blocking, the vaccine effectively inhibited primary tumor growth and induced tumor-specific immune response against tumor recurrence and metastasis of ovarian cancer.

*Corresponding authors.
E-mail addresses: bysyghy@163.com (Hongyan Guo), gaohuile@scu.edu.cn (Huile Gao).
[†]These authors made equal contributions to this work.
Peer review under the responsibility of Chinese Pharmaceutical Association and Institute of Materia Medica, Chinese Academy of Medical Sciences.

https://doi.org/10.1016/j.apsb.2024.06.003

1. Introduction

Ovarian cancer is the fifth leading cause of cancer-related deaths in women and the deadliest gynecologic malignancy[1]. Chemotherapy and surgery are the main clinical strategies for the treatment of ovarian cancer[2,3]. However, these therapies remain ineffective in the treatment of ovarian cancer for several reasons: 1) the majority of patients are diagnosed at an advanced stage with extensive metastases[4], 2) adverse side effects hamper the use of many standard chemotherapeutic agents[5,6], and 3) patients are becoming increasingly multi-drug resistant (MDR) to chemotherapy[7]. Also, scattered tumor cells and residual small tumor tissues during surgery promote metastasis and recurrence of ovarian cancer[8]. Therefore, there is an urgent need to develop new therapeutic strategies to inhibit the progression, recurrence, and metastasis of ovarian cancer.

Immunotherapy has shown great potential in preventing tumor recurrence and metastasis by activating the immune system to enhance anti-tumor immunity and thereby killing tumor cells[9−12]. Among them, tumor vaccines, which are capable of generating specific anti-tumor immune responses, are considered to be one of the most important immunotherapeutic strategies with great therapeutic promise[13−15]. However, tumor vaccines have not achieved the expected clinical results due to the inefficiency of their tumor vaccination cascade process (LDIMP), including antigen recognition and preparation, loading antigens, draining to lymph nodes (LNs), dendritic cell (DC) internalization and maturation, antigen presentation, and T cell activation[16,17]. To improve tumor vaccine efficacy, the vaccine cascade process is optimized, especially antigen preparation, precise vaccine targeting, and remodeling of the immunosuppressive microenvironment leading to enhanced T-cell activation[13,18,19].

Adequate tumor-specific antigen loading is a prerequisite for tumor vaccines to stimulate a strong antigen-specific anti-tumor immune response. Tumor antigens mainly include tumor-associated antigens (TAAs), tumor-specific antigens (TSAs), and whole-cell tumor antigens[13,20]. Due to the co-expression of TAAs on the surface of normal and tumor cells, it is prone to lead to central immune tolerance, which hinders the efficacy and clinical application of TAAs-based tumor vaccines[21]. The process of TSA production, which involves the collection, discovery, and generation of tumor samples, is complex, costly, and time-consuming[22,23]. Due to the presence of broad-spectrum tumor antigens, whole-cell tumor antigens not only circumvent the shortcomings of the above two antigens but also may trigger stronger anti-tumor immune responses, greatly reducing the chances of tumor escape and recurrence[13,24]. However, conventional whole tumor antigens such as whole cell lysates are less immunogenic and are rapidly degraded or cleared *in vivo*[25]. A more effective strategy recently developed is the *in situ* induction of whole-cell tumor antigens, which ablates the tumor *in vivo* and releases tumor antigens to activate tumor-specific immune responses continuously[26]. This strategy often induces immunogenic cell death (ICD) through treatments such as radiation therapy, photothermal therapy, photodynamic therapy, and chemotherapy, prompting the release of paracrine signals from dying cancer cells[25,27,28], followed by the conversion of the tumor into a "vaccine *in situ*", and ultimately, an increase in the type and number of tumor-infiltrating T cells[29,30].

Trametinib (Tra) is a reversible and selective inhibitor of mitogen-activated extracellular signal-regulated kinase 1/2 (MEK 1/2) and inhibits cell proliferation by affecting the MAPK pathway through its action on MEK protein[31]. Recent reports have indicated Tra can induce immune effects *via* ICD, such as the plasma membrane translocation of calreticulin (CRT) and the release of high mobility group box 1 (HMGB1) and ATP[32]. However, Tra treatment would increase the level of the immune checkpoint programmed death ligand 1 (PD-L1)[33], which is always expressed on tumor cells and can connect with programmed death 1 (PD-1) on T cells, leading to the inhibition of activated T cells in the effector phase[34]. Notably, PD-1/PD-L1 blockade has great superiority in combination with Tra-based immunotherapy and remodeling tumor immunosuppressive microenvironment[33]. Meanwhile, in most cases, free antigens induced by ICD are readily and rapidly cleared, and antigen-presenting cells (APCs) are insufficiently activated for antigen processing and presentation, so the resulting antitumor immune response is inadequate[35]. The development of effective platforms that can consistently deliver highly immunogenic *in situ* vaccines in combination with suitable adjuvants and PD-1 blockade is highly desirable.

LNs, as the main organs for innate and adaptive immune responses, are characterized by the presence of a large number of DCs. Therefore, the effective accumulation of vaccines in the LNs is a prerequisite for cancer vaccines to induce robust antigen-specific immune responses[36]. DCs express cell surface-associated mannose receptors. Mannose (Man) modification enhances the recognition of nanoparticles by APCs and their accumulation in LNs[37]. In addition, Man acts as a pathogen-associated molecular pattern (PAMP) to induce phenotypic maturation of DCs in a TLR4-dependent manner[38,39]. Vaccine strategies using Man receptor-mediated internalization have become a well-established option for DC-targeted vaccination[40]. Additionally, nanoparticle size plays a key role in LN drainage[41]. However, previous studies have only selected nanoparticles with a single size to explore LN drainage effects or Man-mediated targeting effects. Therefore, it is of great interest to construct Man-modified nanoparticles with different particle sizes to investigate the effects of particle size on LN drainage, APC capture, and tumor vaccine efficacy.

Smart injected hydrogel as a delivery system for tumor vaccines has attracted attention due to the following advantages: 1) as a carrier to enable the co-loading of multiple actives, such as antibodies, tumor antigens, cytokines, and adjuvants, to collectively enhance the anti-tumor immune response[42]; 2) protecting the active immunomodulators from degradation *in vivo*, which improves the therapeutic bioavailability[43]; and 3) the release behavior of actives in response to various environmental stimuli such as pH, temperature, redox, and enzymes for spatiotemporal specificity[13,16,44,45]. Meanwhile, the tumor microenvironment specifically highly expresses matrix metalloproteinase (MMP)[46]. Thus, the construction of MMP-responsive smart hydrogels can

confer multiple functions to tumor vaccines, including ICD-induced *in situ* antigens, adsorption of antigens by released NPs, targeted delivery of *in situ* vaccines, and sustained MMP-responsive stimulation, which in turn induces potent anti-tumor immune responses.

Herein, we constructed the smart tumor nano-vaccine Tra/CpG@Man-P/Gel to induce potent anti-tumor immune effects and inhibit the primary and metastatic tumors (Scheme 1). First, we prepared Man-modified PLGA nanoparticles with different particle sizes (40, 100, 200 nm) and encapsulated the immune adjuvant CpG to activate TLR9[47]. MMP-responsive gels were prepared by using the addition reaction of 4-arm-PEG-Mal with MMP-2-responsive peptides[48], to co-coagulate CpG@Man-P and Tra to realize the sustained *in situ* antigen production, LN drainage, and APCs presentation, which in turn activated anti-tumor immune responses. CpG@Man-P (40 nm) exhibited superior release of nanoparticles and drugs, superior LN targeting, and more accumulation than nano-adjuvants with larger sizes. Therefore, we choose CpG@Man-P (40 nm) as the model nano-adjuvant to investigate the antitumor and anti-metastasis effects. Finally, the anti-tumor and anti-metastatic effects of the in-situ vaccine Tra/CpG@Man-P/Gel combined with PD-1 antibody were explored by an ovarian cancer model. The simple production process and the ability to simultaneously induce patient-specific immune responses and counteract immune tolerance hold promise as a potent cancer vaccine for combinational immunotherapy.

2. Materials and methods

2.1. Materials, cell lines, and animals

4-Aminophenyl-α-D-mannopyranoside was obtained from J&K Scientific (Beijing, China). Polylactic acid-hydroxyacetic acid copolymer (PLGA, LA: GA = 50:50, Mw = 10 kDa) was purchased from Xi'an Ruixi Biological Technology (Xi'an, China). 3-(4,5-Dimethylthiazol-2-yl)-2,5-diphenyltetrazolium bromide (MTT) assay kit and collagenase IV were purchased from Biofroxx (Einhausen, Germany). 4-Arm-PEG-Mal was obtained from Ponsure Biological (Shanghai, China). Fluorescent dye-conjugated anti-CD86, anti-CD80, anti-CD3, anti-CD4, anti-CD8, anti-Foxp3, and anti-CD11c mouse antibodies were purchased from Biolegend (San Diego, CA, USA).

Murine ID8 ovarian cancer cells and DC2.4 cells were obtained from the Chinese Academy of Sciences Cells Bank (Shanghai, China). Complete RPMI-1640 or DMEM cell culture medium (containing 10% of fetal bovine serum, 100 U/mL of penicillin G, and 100 U/mL of streptomycin sulfate) was prepared to culture cells. Cells were retained in an incubator under a condition of 37 °C and 5% CO_2.

Female C57 mice (5−6 weeks, 18−22 g) were obtained from SiPeiFu Biotechnology Co., Ltd. (Beijing, China). All experimental procedures were executed according to the protocols approved by the Ethics Committee of Peking University Third Hospital (License No. IRB00006761-M2019291).

2.2. Synthesis of Man-PLGA

The carboxylic acid terminal group of PLGA was modified with 4-aminophenyl-α-D-mannopyranoside (Man) in a mild nitrogen atmosphere. PLGA (0.0133 mmol, 1 equiv.) was dissolved in dimethylformamide and activated by 4-dimethylaminopyridine (0.05 mmol, 4 equiv.) and *N*,*N*′-dicyclohexylcarbodiimide (0.027 mmol, 2 equiv.) at room temperature for 2 h. 4-Aminophenyl-α-D-mannopyranoside (0.027 mmol, 2 equiv.) was added to the above solution and stirred at room temperature for 48 h. The polymer was precipitated with water

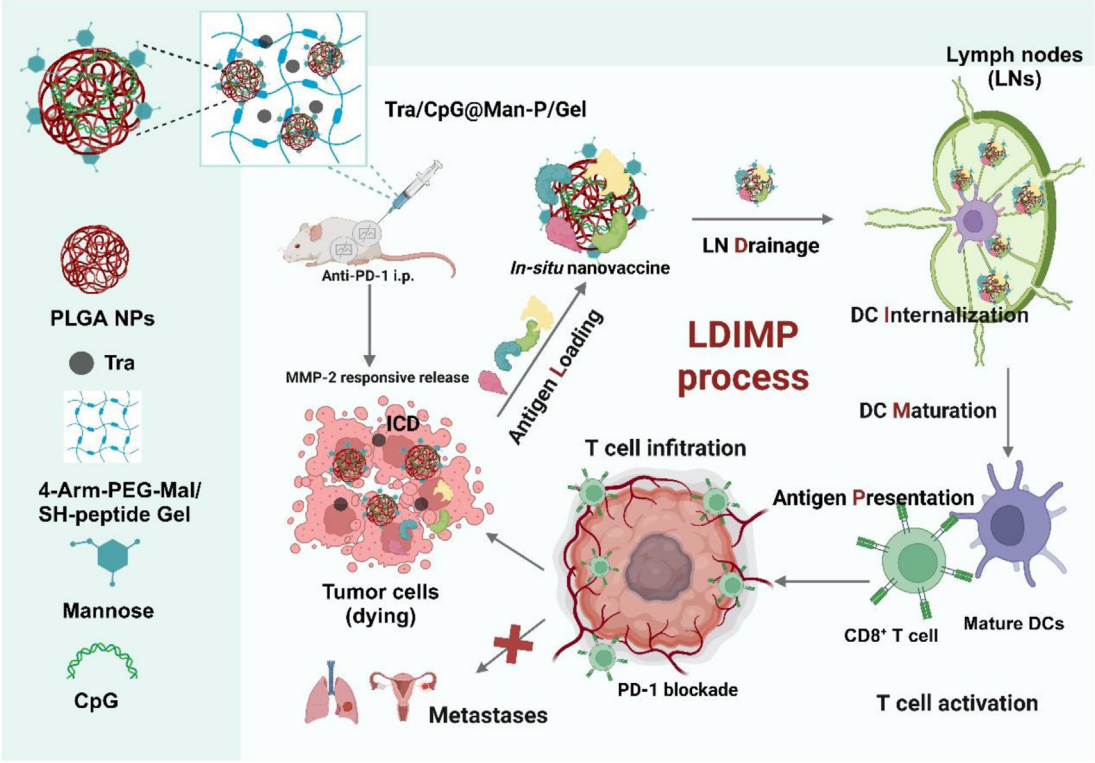

Scheme 1 Scheme illustration of Tra/CpG@Man-P/Gel *in situ* nano-vaccine system and improved LDIMP process.

and recovered by centrifugation. Man-PLGA was dissolved in dichloromethane and dried over anhydrous sodium sulfate. Filter the solution. The DCM was rotary evaporated methanol was added to precipitate the polymer and the crude reaction solution was washed. Dissolve Man-PLGA in DCM and repeat the precipitation process. Finally, man-PLGA was dried under a vacuum overnight.

2.3. Synthesis and characterization of multi-sized nanoparticles

10 μg of CpG was dissolved in 100 μL of PBS, and the solution was added to 1 mL of acetone-dichloromethane (1:1, *v/v*) dissolved in 10 mg/mL Man-PLGA as the organic phase in an ice bath, and sonicated for 2 min using an ultrasonic probe at 20% power. The mixture was added to 5 mL of 5% PVA (203) solution and sonicated in an ice bath for 5 min at 40% power to form an emulsion. The organic solvent was removed by evaporation under reduced pressure at 37 °C to obtain CpG@Man-P (40 nm). CpG@Man-P (100 nm) and CpG@Man-P (200 nm) were prepared similarly by changing the power and time of the second sonication. The sizes and zeta potential of nanomedicines were monitored by dynamic light scattering (DLS, Brookhaven, USA). The morphology and particle size of these nanoparticles were observed by transmission electronic microscopy (TEM, H-600, Hitachi, Japan).

2.4. Determination of encapsulation rate and drug loading

The encapsulation of CpG by Man-P (40, 100, 200 nm) was verified by agarose gel electrophoresis. The absorbance values were determined by using a UV absorption spectrophotometer, and the encapsulation ratio of the nanoparticles and drug loading was calculated from the standard curve of CpG. The Drug loading ratio (DL) and Entrapment ratio (ER) were calculated according to Eqs. (1) and (2):

$$\text{DL}\,(\%) = \text{Mass of encapsulated drug}/(\text{Total mass of carrier and encapsulated drug}) \times 100 \quad (1)$$

$$\text{ER}\,(\%) = \text{Mass of encapsulated drug}/\text{Total mass of drug} \times 100 \quad (2)$$

2.5. Gels preparation

4-Arm-PEG-Mal and thiol-containing peptides (Mal/SH molar ratio of 1:1.1) were dissolved into TEA buffer to obtain the prepolymer solution. Multi-sized nanoparticles CpG@Man-P (40, 100, 200 nm), and trametinib (Tra) were sequentially added to the prepolymer solution, vortexed to mix thoroughly, and heated at 37 °C for 30 min until the gel no longer flowed. Drug-loaded gels Tra/CpG@Man-P/Gel containing different-sized nano-adjuvants were obtained, respectively. Blank gels were prepared in the same way except that trametinib was not added.

2.6. Characterization of gels

The prepared drug-loaded gels Tra/CpG@Man-P/Gel were freeze-dried and the volume change of the gels was observed. The freeze-dried gels were cut into small pieces of about 3 mm^2 and imaged by scanning electron microscope (SEM, SU3500, Hitachi, Japan) to observe the pore structure inside the gels.

The equilibrium swelling ratios (Swelling ratio, SR) of multi-sized drug-loaded gels Tra/CpG@Man-P/Gel were determined by gravimetric method. A certain weight (150 mg, m_0) of the gels was immersed in 10 mL of PBS at 37 °C. At a predetermined time, the gel mass (m_t) was determined after removing free water from the gel surface with filter paper. Three parallel samples were performed for each experiment. SR can be calculated using Eq. (3):

$$\text{SR}\,(\%) = (m_t - m_0)\ /\ m_0 \times 100 \quad (3)$$

The rheological properties of Tra-encapsulated gels and blank gels were tested by rheological instrumentation. To study the viscoelastic properties of the gels, the storage modulus (G'), and loss modulus (G'') of the gel samples were measured at different angular frequencies.

2.7. MMP-2 responsiveness

MMP-2 enzyme was diluted to 100 μg/mL with assay buffer, and incubated at 37 °C for 1 h to activate. Hydrogels with exact mass (m_0) were placed in different buffer media (PBS, PBS with 100 ng/mL MMP-2, PBS with 200 ng/mL MMP-2, PBS with 400 ng/mL MMP-2) and incubated at 37 °C. After 5 days, the samples were taken out of the buffer, rinsed with distilled water, and vacuum-dried to obtain the mass of the degraded gel (m_t). The mass loss rate of gel was calculated as Eq. (4):

$$\text{Mass loss rate}\,(\%) = (m_0 - m_t)\ /\ m_0 \times 100 \quad (4)$$

2.8. Drug release

CpG@Man-P was fluorescently labeled using Dil (40 nm, 100 nm, 200 nm). Dil solution was added to acetone-dichloromethane (1:1, *v/v*, 1 mL) dissolved with 10 mg/mL Man-PLGA (LA: GA = 50:50, Mw = 10 kDa) as the organic phase, and 100 μL of PBS was added to the organic phase, and the remaining procedure was the same as the synthesis method of CpG@Man-P. After the preparation, PVA and free Dil were removed using a 100 kDa ultra-rate tube.

Gels containing different Dil fluorescently labeled particles and Tra were prepared. The gels were incubated with MMP-2 (200 ng/mL) concentration, at 37 °C, pH 6.8. Sequentially, 1 mL of liquid was taken out at 2, 4, 6, 8, 16, 24, 48, 72, 96, and 120 h time points, and the release of particles was measured by fluorescent intensity under 542 nm excitation and 564 nm emission, respectively. UV−Vis absorbance at 360 nm was measured to calculate the release of Tra.

2.9. Antigen absorption by Man-P

Total protein from ID8 cells was extracted by using an animal tissue/cell total protein extraction kit (column method, Solarbio, Beijing, China). Briefly, the centrifuge column and its receiver tube sleeve were pre-cooled on ice. To wash the ID8 cells, pre-cooled PBS was added to the Petri dish with slight shaking, and the supernatant was discarded. Subsequently, the corresponding volume of RIPA cell lysate was added and blown several times repeatedly, and the lysed cells were transferred to the pre-cooled centrifuge column casing and centrifuged (14,000−16,000 rpm, 30 s), after which the collection tubes were immediately placed on

ice and the centrifuge column was discarded. CpG@Man-P (40 nm/100 nm/200 nm) nanoparticles were incubated with ID8 proteins for 1 h at 37 °C. CpG@Man-P nano-adjuvants adsorbed with antigenic proteins were separated by size exclusion chromatography (Sepharose CL-4B, Sigma−Aldrich, St. Louis, MO, USA) and concentrated ultrafiltration. Then, the total protein amount and the size change were measured to confirm the antigen adsorption. The antigen proteins attached to the nanoparticles were mixed with protein loading buffer, boiled to denature, separated by commercially available 4%−15% polyacrylamide gradient gels and finally visualized by Caumas Brilliant Blue staining.

2.10. Biocompatibility in vitro

The MTT method was used to investigate the safety of CpG@Man-P (40, 100, 200 nm) with different particle sizes for DC cells. DC 2.4 cells were inoculated in 96-well plates at a concentration of 3×10^3 cells/well. 12 h later, 40, 100, and 200 nm CpG@Man-P were added at a concentration of 20 μg/mL, respectively. After incubation for 24 h, the culture medium was replaced with 1640 medium containing 0.5 mg/mL MTT, and incubated for another 4 h at 37 °C, and then aspirated. 100 μL of DMSO solution was added to each well, and the UV absorption value at 570 nm was detected by using an enzyme labeling instrument (PerkinElmer) after shaking at a constant temperature of 37 °C for 20 min. The cellular survival rate was calculated. Cytotoxicity of Tra was evaluated using MTT assay as mentioned above.

2.11. ICD effect in vitro

ID8 cells (5×10^4 per well) were seeded in 12-well plates and grew for 24 h. The cells were incubated with Tra (10, 20 μg/mL) for 24 h. The translocation of CRT was measured by flow cytometry and observed by fluorescent microscope (CLSM, Leica, Wetzlar, Germany). Moreover, the supernatant was collected to test the contents of released ATP.

2.12. Biodistribution

5×10^6 ID8 cells were dispersed in a 50:50 mixture of PBS and matrix gel, and injected subcutaneously into the right side of the back of mice. When the tumors grew to approximately 200 mm^3, the mice were randomly divided into 6 groups ($n = 6$). CpG@Man-P (40, 100, 200 nm) and CpG@P (40, 100, 200 nm) nanoparticles were labeled with DiR and encapsulated in gels. 100 μL of gels were intratumorally injected into mice. Fluorescence changes at tumor sites were observed with the IVIS system at 2, 4, 12, 24, 36, and 72 h post-injection. After the last imaging, the mice were sacrificed, and the tumors, major organs, and lymph nodes were collected to obtain an *ex vivo* fluorescence image.

2.13. Cellular uptake

DC 2.4 cells and BMDCs were seeded in 12-well plates at a density of 8×10^5 per well and grew for 24 h to obtain 80% confluency. Dil-labeled CpG@Man-P (40, 100, 200 nm) and CpG@P (40, 100, 200 nm) nanoparticles in fetal bovine serum-free medium were added into the well and further incubated for 4 h, respectively. The fluorescence of Dil was measured by flow cytometry (Agilent NovoCyte, Santa Clara, USA) and captured using a confocal laser microscope (CLSM, Leica, Wetzlar, Germany).

2.14. DC maturation

DC 2.4 cells (5×10^4) and BMDCs (8×10^5) were planted in 12-well plates and cultured for 24 h. The cells were treated with CpG@Man-P (40 nm, 100 nm, 200 nm), Man-P, CpG, and lipopolysaccharide (LPS, 1 μg/mL, as positive control) for 48 h. Mature DCs expressed maturation markers (CD80 and CD86), which were analyzed by flow cytometry (Agilent NovoCyte, Santa Clara, USA).

2.15. T cell proliferation in vitro

BMDCs were inoculated in 12-well plates at a density of 5×10^4 cells per well and incubated for 24 h. BMDC were co-incubated with CpG@Man-P (40, 100, 200 nm), CpG, (CpG = 2 μg/mL), and LPS (1 μg/mL) for 48 h, respectively. $CD8^+$ T cells were isolated from the splenocytes of C57 mice, labeled with CFSE, and then added into each well. After incubating for 3 days, all cells were collected and stained with anti-CD8 antibody. T cell proliferation was evaluated by quantification of $CD8^+$ T cells and CFSE dilution.

2.16. Evaluation of remote effects

Female C57BL/6 mice were injected subcutaneously in the left shoulder with 1×10^7 cells (primary tumor) and in the right shoulder with 5×10^6 cells (distant tumor). When the primary tumor volume reached about 50 mm^3, the mice were randomly divided into PBS, Tra/Gel, CpG@Man-P/Gel, and CpG@Man-P/Tra/Gel + PD-1 groups, with 8 mice in each group (Tra = 1.25 mg/kg, CpG@Man-P = 5 mg/kg, anti-PD-1 = 100 ug per mouse). The tumor volume and body weight were recorded every 2 days. The mice were intratumorally injected with various formulations every 7 days. After the last administration, the mice were sacrificed and the tumors and major organs were collected for HE staining and immunofluorescence analysis. Tumors, spleens, and lymph nodes were further processed into single-cell suspensions for evaluation of anti-tumor immune responses.

2.17. Anti-metastasis effect in vivo

Female C57BL/6 mice were injected subcutaneously in the left shoulder with 5×10^6 cells (metastatic tumor). The tumor volume was determined every day. The mice bearing metastatic tumors around 50 mm^3 were randomized to PBS, Tra/Gel, CpG@Man-P/Gel, and CpG@Man-P/Tra/Gel + PD-1 groups. The dosing regimen and dosage were consistent with the above. Meanwhile, the mice were intraperitoneally injected with 5×10^6 cells. After the last treatment, the mice were sacrificed, and the major organs and tumors were collected and fixed. The lung metastasis nodes were calculated as $I \times 1 + II \times 2 + III \times 3 + IV \times 4 + V \times 5 + VI \times 10$ (grade I < 0.5 mm; 0.5 mm ≤ grade II < 1 mm; 1 mm ≤ grade III <2 mm; 2 mm ≤ grade IV < 3, 3 mm ≤ grade IV < 5, VI > 5 mm).

2.18. Statistical analysis

One-way analysis of variance (ANOVA) or *t*-test for multiple comparisons was used for statistical analysis. All data were

expressed as mean ± standard deviation (SD). Statistical significance was set at $*P < 0.05$, $**P < 0.01$, $***P < 0.001$, and $****P < 0.0001$.

3. Results and discussion

3.1. Preparation and characterization of nanoparticles

First, Man-PLGA was successfully synthesized and characterized by FTIR spectroscopy (Supporting Information Fig. S1A). Compared with the parent PLGA, Man-PLGA showed obvious absorption peaks near 700 cm^{-1}, which belonged to the C−H surface bending vibration of the benzene ring. These peaks are similar to the absorption peaks of Man near 700 cm^{-1}, indicating that Man-PLGA was successfully synthesized.

CpG-loaded nanoparticles with different sizes were prepared and characterized. Dynamic laser scattering (DLS) measurements revealed that hydrodynamic diameters of prepared CpG@Man-P nanoparticles were 44.1, 111.9, and 210.1 nm, respectively (Fig. 1A−C), which were noted as CpG@Man-P (40 nm), CpG@Man-P (100 nm), and CpG@Man-P (200 nm), respectively. Transmission electronic microscopy (TEM) further showed the uniform distribution of nanoparticles with spherical morphology (Fig. 1A−C). Agarose gel electrophoresis confirmed the successful loading of CpG without free CpG (Fig. S1B). Moreover, the drug loading capacity and encapsulation efficiency of CpG were around 0.08% and 78%, respectively, being measured by ultraviolet spectrophotometry (Supporting Information Table S1).

3.2. MMP-2 sensitive drug release gel system

Through Michael addition reaction, 4-arm-PEG-Mal was made to cross-link with thiol-containing peptides thus obtaining gel systems containing CpG@Man-P nanoparticles of different sizes and Tra. As shown in Supporting Information Fig. S2A, the mixture solution of drug, nanoparticles, 4-arm-PEG-Mal, and MMP-2 responsive peptide turned to be viscous and turbid, turned into gel after incubation at 37 °C for 30 min. The SEM image showed that the fabricated gels showed an interconnected porous multilayer network structure, with pore sizes distributed between 50 and 100 μm (Fig. 1D). The storage modulus G' and loss modulus G'' of the prepared gels at different angular frequencies were determined by rheological apparatus. As can be seen from Fig. S2B, the loss modulus of each group did not show significant differences. For the storage modulus, the group of gels containing CpG@Man-P (200 nm) had the highest G' value, indicating a more effective intermolecular cross-linking density and higher mechanical properties. In addition, the G' of all groups was higher than that of the control Gel group, which also reflected the enhanced mechanical properties of the drug-loaded gels. Meanwhile, FTIR spectra showed that the −C═C peak of 4-arm-PEG-Mal disappeared after gelation, indicating that the gel was formed by the Michael addition reaction (Fig. S2C). Moreover, the prepared gels showed rapid swelling by 15 h (Fig. 1E). The gel containing CpG@Man-P (100 nm) reached equilibrium swelling first at 15 h, and the remaining three groups reached equilibrium at about 24 h. The equilibrium swelling rates of the gels in the Tra/Gel, Tra/CpG@Man-P/Gel (40 nm), Tra/CpG@Man-P/Gel (100 nm), and Tra/CpG@Man-P/Gel (200 nm) groups were about 228%, 304%, 246%, and 280%, respectively. The swelling rate of the gel group containing nanoparticles was generally higher than that of the Tra/Gel group, but the difference between the gel groups containing different sizes of CpG@Man-P (40, 100, 200 nm) was not significant. This suggested that the encapsulation of nanoparticles may slightly increase the swelling rate of the gels, but the change in the size of the particles did not significantly affect the swelling properties of the gels.

3.3. MMP-2 responsive capacity

As expected, the Tra-loaded gels would disintegrate in the presence of MMP-2. Incubated with 100, 200, and 400 ng/mL of MMP-2 for 5 days, the gels lost about 47%, 59%, and 93%, respectively, indicating the MMP-2 responsive degradation of gels (Fig. 1F). In addition, a concentration of 200 ng/mL of MMP-2 enzyme was selected for study in subsequent experiments according to the mass loss rate. Then, the responsive release of nanoparticles and Tra was also measured. The nanoparticles were labeled with fluorescent dye Dil to track the release of CpG@Man-P from gels. The gels treated with MMP-2 displayed more rapid release of CpG@Man-P and Tra, compared to corresponding control gels (Fig. 1G and H), benefiting from MMP-2-triggered degradation of gels. Meanwhile, the release rate decreased with the size increase of nanoparticles, suggesting that large-sized nanoparticles may be difficult to release completely from the gel system. These results jointly verified the MMP-2 responsive capacity of gels and the MMP-2-controlled release of nanoparticles and drugs.

3.4. Improving the LDIMP process

Firstly, we excluded the effect of nanoparticles on cell viability, and DC2.4 cells were seeded for the cytotoxicity assay to investigate the biosafety of nano-adjuvants (Supporting Information Fig. S3). The results confirmed that the proliferation of normal cells was not influenced by nano-adjuvants even at a high concentration (1 mg/mL). The tumor antigens were generated by stimulation of Tra released from gels, which induced potent ICD. MTT assay of Tra on ID8 cells showed a concentration-dependent killing effect with an IC_{50} around 20.84 μg/mL (Supporting Information Fig. S4). Next, the ICD of ID8 cells was investigated by measurement of released ATP and translocation of CRT on the cell surface. There was increased CRT exposure on the cell surface treated with Tra (Fig. 2A, and Supporting Information Fig.S5). Similarly, the amount of released ATP increased with the concentration of Tra increase (Fig. 2B). Quantification results also verified that the cells treated with Tra translocated more CRT from endoplasmic reticulum to cell membrane (Fig. S5A and S5B), which increased with concentration increase. The data jointly demonstrated that the Tra-containing nano vaccinations could induce the ICD of tumor cells and generate whole-cell tumor antigens.

Antigen adsorption is one of the important functions of immune nanoparticles, and the antigen adsorption ability of CpG@Man-P was further investigated by SDS-PAGE electrophoresis studies. It was observed that CpG@Man-P (40, 100, 200 nm) had similar characteristic bands compared with the TP group (Supporting Information Fig. S6A), indicating that CpG@Man-P successfully captured the total ID8 antigen protein. The antigen adsorption amounts of CpG@Man-P (40 nm), CpG@Man-P (100 nm), CpG@Man-P (200 nm) were measured to be around 6.78, 8.22, 12.68 μg/mg, respectively, by the BCA protein quantification (Fig. 2C), indicating that the increase in the particle size of CpG@Man-P might contribute to the better

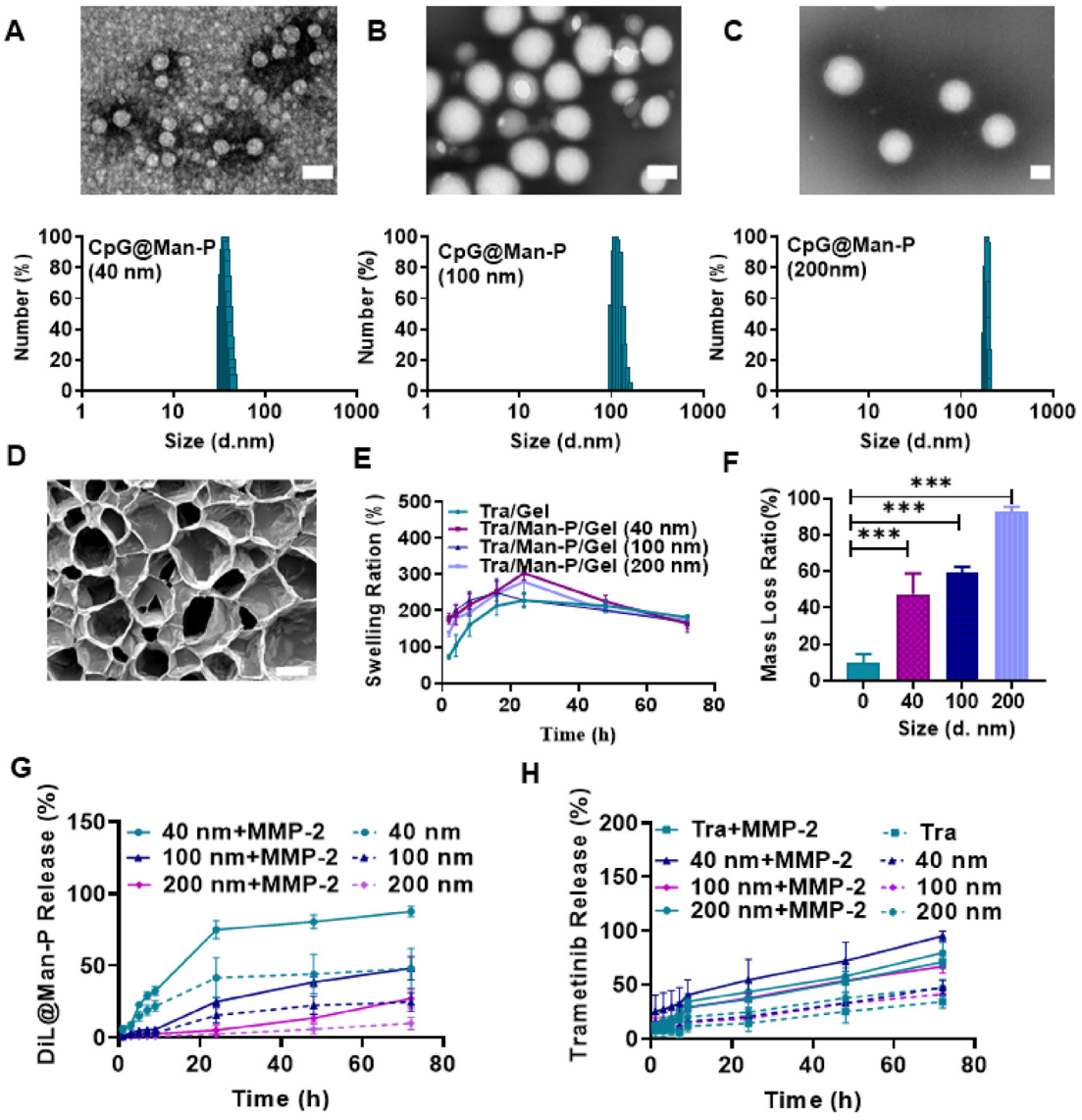

Figure 1 Preparation and characterization of Tra/CpG@Man-P/Gel system. (A−C) TEM images and DLS measurements of CpG@Man-P (40 nm/100 nm/200 nm). Scale bars represent 100 nm. SEM image (D), swelling ratio (E), and mass loss ratio (F) of prepared gel systems. Error bars represent mean ± SD ($n = 3$). Statistical significance was set at $^{*}P < 0.05$, $^{**}P < 0.01$, $^{***}P < 0.001$, and ns, not significant. The scale bar represents 50 μm. (G, H) Cumulative release profiles of Dil@Man-P NPs with different sizes and Tra from nanogels incubated with MMP-2.

adsorption of antigen. In addition, the nanoparticle size after adsorption of antigen increased to 63.18, 158.45, and 228.41 nm, respectively (Fig. S6B), which also verified that nano-adjuvants successfully adsorbed the whole-cell tumor antigens.

Then, we confirmed whether nanoparticles migrated to and accumulated in LNs after responsive release from gels, by using *in vivo* imaging system (IVIS). The tumors and major LNs were collected to obtain *ex vivo* fluorescence imaging post at 24 h and 48 h intra-tumoral injection. Man-modified nano-adjuvants exhibited better LN targeting and accumulation compared to unmodified nano-adjuvants, which was consistent with previous research (Fig. 2D and E). Meanwhile, there was more accumulation in tumors of nano-adjuvants without Man modification (Supporting Information Fig. S7). Moreover, CpG@Man-P (40 nm) exhibited a better ability of LN targeting and accumulation than nano-adjuvants with a larger size, which would induce a stronger antitumor immune response. This might be because that small particle size could facilitate more efficient drainage to the LNs.

It is well known that the maturation of DCs plays a vital role in T cell activation. First, we evaluated the cellular uptake of nano-adjuvants on bone marrow-derived DCs (BMDCs) and DC2.4 cells, detected by flow cytometry and fluorescence microscopy. There was a stronger fluorescence signal in CpG@Man-P treated cells than cells treated with CpG@P without Man modification (Fig. 2F, Supporting Information Fig. S8A and S8B), suggesting that the Man modification could heavily improve the uptake of NPs by DCs, due to the overexpression of Man receptors on DCs. Meanwhile, the CpG@Man-P (200 nm) treated group exhibited the highest uptake compared to the CpG@Man-P (40 nm) and CpG@Man-P (100 nm) groups, which may be related to the high phagocytosis capacity of the DCs for larger particles.

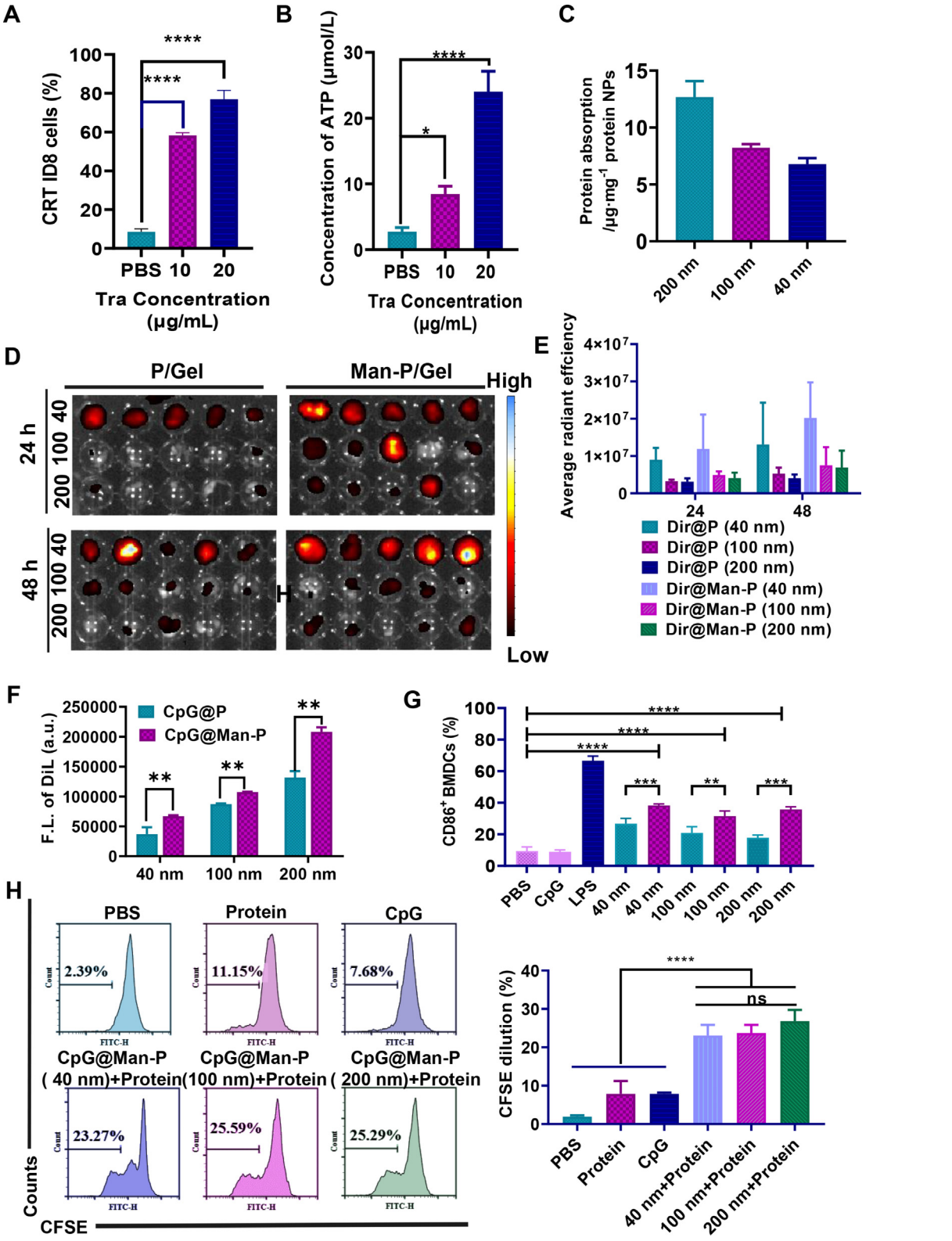

Figure 2 Tra/CpG@Man-P/Gel motivated antigen LDIMP process. (A) CRT exposure on the surface and (B) extracellular ATP of ID8 cells treated with Tra. (C) Quantification of proteins absorbed by nano-adjuvants with different sizes. (D, E) *Ex vivo* fluorescent images (D) and semi-quantitative results (E) of major LNs collected at 24, and 48 h post intratumoral injection. Data are presented as mean ± SD ($n = 3$). (F) Cellular uptake of Dil@P and Dil@Man-P by BMDC cells. (G) The percentages of $CD86^+$ BMDCs after incubation with different formulations. (H) The percentages of CFSE dilution-gated $CD8^+$ T cells after different treatments. Error bars represent mean ± SD ($n = 3$). Statistical significance was set at $^*P < 0.05$, $^{**}P < 0.01$, $^{***}P < 0.001$, $^{****}P < 0.0001$, and ns, not significant.

To activate T cells and antitumor immune response, immature DCs are supposed to differentiate into mature DCs and generate co-stimulatory signals and cytokines. CD80 and CD86 belong to a family of costimulatory molecules that play an important role in the immune system, which are often recognized as markers of maturation and activation of DCs. Then, the capacity of nano-adjuvants to maturate DCs was investigated in DCs and BMDCs by detecting the percentages of $CD80^+$ DCs and $CD86^+$ DCs. The application of CpG is limited by rapid extracellular and intracellular enzymatic degradation and poor uptake by DCs in blood and lymphatic circulation. Therefore, free CpG induced negligible DC maturation (Fig. 2G, and Fig. S8C−S8E). Man-modified NPs showed a slight immune stimulation effect on promoting DC maturation compared to the PBS group. In contrast, CpG-loaded nano-adjuvants exhibited obvious increased percentages of mature ($CD86^+$ or $CD86^+$) DCs, benefiting from protection from enzymatic degradation by encapsulation. All results indicated that CpG@Man-P could heavily promote DC maturation in a TLR-9/TLR4-dependent manner, due to CPG loading and Man modification.

Finally, the activation of T cells was further investigated at the cellular level. Naïve T cells become devoted to a clonal expansion and differentiation into effector T cells when receiving the antigenic and co-stimulatory signals, displaying an increase in cell number. The whole-cell antigens and free CpG could slightly improve the proliferation of $CD8^+$ T cells. In contrast, *in situ* nano-vaccines, consisting of nano-adjuvant (CpG@Man-P) and whole-cell antigens (Protein), could significantly activate $CD8^+$ T cells and promote $CD8^+$ T cell proliferation almost 12 folds more than the PBS group (Fig. 2H). All the data demonstrated that the Tra/CpG@Man-P/Gel could induce ICD of tumor cells to generate whole-cell antigens, further form *in situ* nano-vaccines to drain to LNs and be internalized by DCs to mature DCs, and finally stimulate T cells to activate and proliferate.

3.5. *Antitumor effect evaluation of in situ vaccines*

According to the results of the LDIMP process, the CpG@Man-P (40 nm) nano-adjuvants were selected to prepare *in situ* nano-vaccines to evaluate the antitumor effect *in vivo*. Additionally, PD-1 blockade was further employed to improve antitumor immunity. Briefly, the mice bearing ID8 tumors were randomized into five groups and treated with PBS, CpG@Man-P/Tra, Tra/Gel, Tra/CpG@Man-P/Gel, and Tra/CpG@Man-P/Gel + anti-PD-1, respectively (Fig. 3A). After the last administration, the mice were sacrificed and the major organs and tumors were collected for further investigation. Tra/CpG@Man-P/Gel and Tra/CpG@Man-P/Gel + anti-PD-1 groups showed similar growth volume and tumor inhibition of primary tumors, with the highest inhibition rate (Fig. 3B−D, Supporting Information Fig. S9A). In contrast to Tra/Gel, all the CpG-containing groups displayed better antitumor effects, owing to the in-situ generation of whole-cell antigens and CpG-mediated immunomodulation. Meanwhile, Tra/CpG@Man-P/Gel and Tra/CpG@Man-P/Gel + anti-PD-1 groups exhibited strong suppression on distant tumors, better than single immunomodulator or chemotherapeutic drug-loaded groups (Fig. 3E). The volume of distant (left) tumors exhibited similar growth curves with primary tumors (Fig. 3F, Fig. S9B), and the results of distant tumor inhibition rate were well consistent with the results of primary tumors (Fig. 3G). The quantification results of primary and distant tumor weights also indicated the superior antitumor effect of in-situ nano-vaccines Tra/CpG@Man-P/Gel and combination with PD-1 blockade (Fig. 3H and I), suggesting that the improved LDIMP process could enhance antitumor immunity. Moreover, there was no obvious body weight loss in mice (Fig. 3J) and the H&E images of major organs showed insignificant damage, indicating the biosafety of nano-vaccines (Supporting Information Fig. S10).

Then, the LN, spleen, and tumor were collected to determine the antitumor immune responses. Firstly, the percentages of matured DCs, $CD8^+$ T cells, and $CD4^+$ T cells were detected by flow cytometry (Fig. 4A−D). There was the highest frequency of $CD80^+$ and $CD86^+$ DCs in the LNs of Tra/CPG@Man-P/Gel treated mice, whose percentages of $CD80^+$ DCs and $CD86^+$ DCs were 2.0- and 2.3-fold higher than CpG@Man-P/Gel groups, respectively (Fig. 4A and B). The quantitative results of $CD80^+$ and $CD86^+$ DCs showed similar results (Fig. 4E and F). Tra/CpG@Man-P/Gel and Tra/CpG@Man-P/Gel + PD-1 showed similar levels of DC maturation, higher than CpG@Man-P/Gel and Tra/Gel, benefiting from the generation of *in situ* antigens and nano-adjuvants-mediated antigen presentation and DC maturation. Meanwhile, there were more $CD4^+$ T cells and $CD8^+$ T cells in the LNs of Tra/CpG@Man-P/Gel and Tra/CpG@Man-P/Gel + PD-1 groups than in other groups, indicating the stronger activation and proliferation of T cells (Fig. 4B, C, G and H). Meanwhile, there were more $CD4^+$ T cells and $CD8^+$ T cells in the spleens of mice treated with Tra/CpG@Man-P/Gel than other groups, whose percentages of $CD4^+$ T cells and $CD8^+$ T were 1.2-fold and 1.8-fold higher than CpG@Man-P/Gel, respectively (Fig. 5A, B, E and F). Moreover, the abundance of immunosuppressive cells (T_{reg} cells) in spleens was determined at the same time (Fig. 5G). Tra/CpG@Man-P/Gel treatment could improve the Treg number in a negative feedback manner, which was downregulated by PD-1 blockade. DC maturation in spleens was also evaluated (Fig. 5C, D, H and J). Briefly, there were more DC cells and stronger DC maturation in the spleens of Tra/CpG@Man-P/Gel group, owing to a combination of *in situ* generation of tumor antigens and LN-targeting nano-adjuvants.

Next, infiltrating T cells of primary and distant tumors were determined. We first detected the T cell classification in primary tumors. There were heavily improved $CD4^+$ T cells and $CD8^+$ T cells in CpG@Man-P containing groups, compared to the PBS group (Fig. 6A and B), indicating enhanced antitumor immunity. Moreover, Tra-containing treatments induced obvious PD-L1 upregulation in primary tumors (Fig. 6C), indicating the necessity of combination with PD-1 blockade. As respected, there were downregulated T_{reg} cells in the primary tumors of mice treated with *in situ* nano-vaccines (Fig. 6D). Tra/CpG@Man-P/Gel + PD-1 treatment reduced the proportion of T_{reg} cells by nearly 2.5-fold compared to the PBS group in primary tumors indicating that the combination with PD-1 blockade would inverse the immunosuppressive microenvironment and enhance the antitumor immune response induced by *in situ* nano-vaccines. Meanwhile, the abundance of T cells in distant tumors was also investigated by flow cytometry. As expected, there was a great deal of $CD4^+$ T cells and $CD8^+$ T cells infiltrating the distant tumors of mice treated with CpG@Man-P containing formulations (Fig. 6E and F), indicating great antitumor immunity. Moreover, the frequency of $PD\text{-}L1^+$ cells and T_{reg} cells in distant tumors was detected, which was well consistent with the results of primary tumors (Fig. 6G and H). Tra/CpG@Man-P/Gel + PD-1 treatment reduced the percentage of T_{reg} cells by nearly 13.1-fold compared to the PBS group. Together, these results indicated that the in-situ nano-vaccines

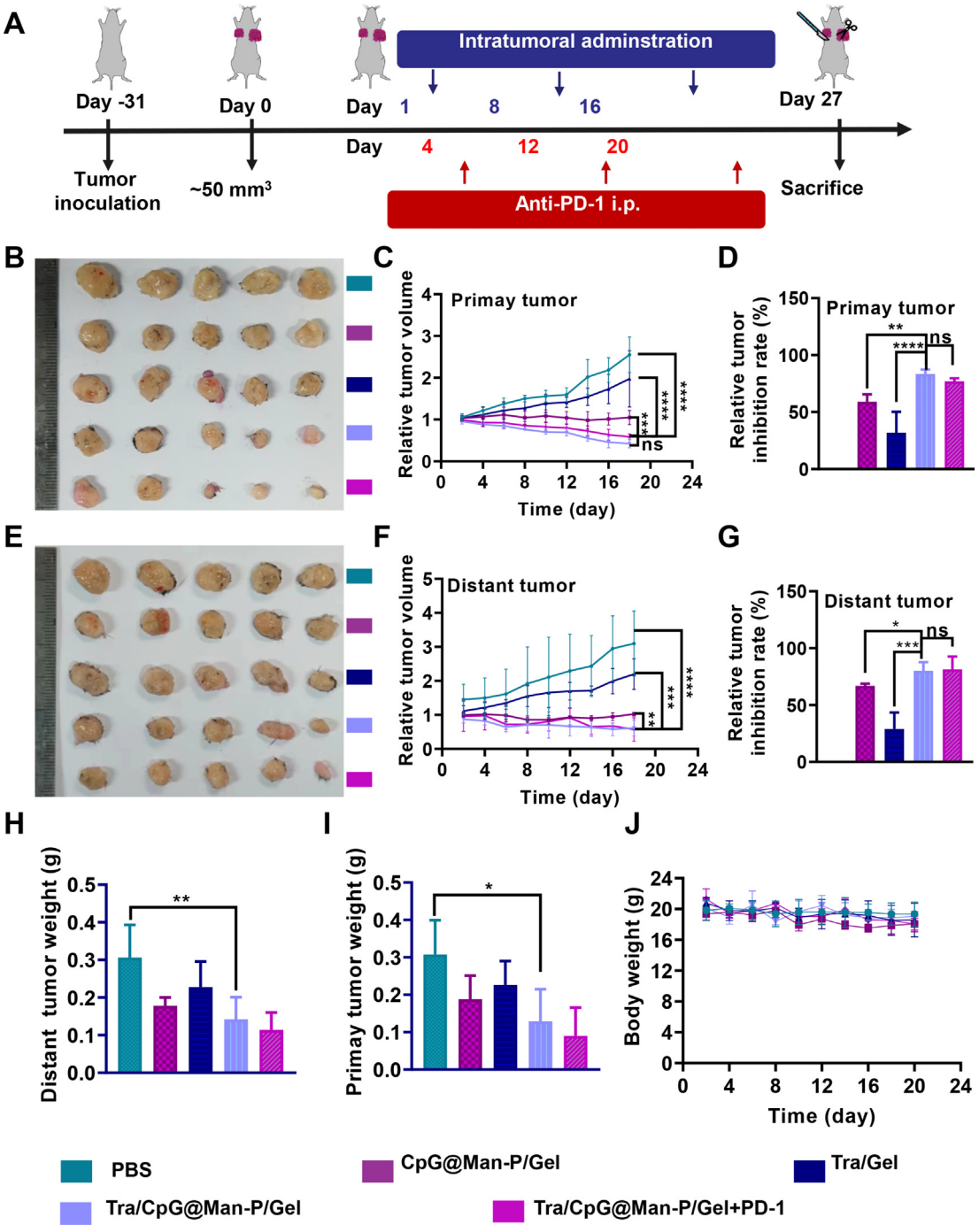

Figure 3 Antitumor effects and remote effects in ID8 tumor models. (A) Schematic depicting the experimental approach. (B−D) Representative images (B), relative tumor growth curve (C), and tumor inhibition ratio (D) of primary tumors after treatment. (E−G) Representative images (E), relative tumor growth curve (F), and tumor inhibition ratio (G) of distant tumors after treatment. Weigh of primary (H) and distant tumors (I). (J) The body weight of mice was recorded every two days. Error bars represent mean ± SD ($n = 5$). Statistical significance was set at $^{*}P < 0.05$, $^{**}P < 0.01$, $^{***}P < 0.001$, $^{****}P < 0.0001$, and ns, not significant.

Tra/CpG@Man-P/Gel could not only suppress the development of primary tumors but also distant tumors, due to improved LDIMP process, whose efficiency was further enhanced by PD-1 blockade.

Finally, the levels of cytokines in the primary and distant tumors were evaluated to investigate the immune response in the ID8 tumor model (Supporting Information Fig. S11). There were upregulated pro-inflammatory factors, including IFN-γ, IL-6, IL-1β, and TNF-α, in both primary and distant tumors of mice treated with nano-adjuvant/Tra-containing formulations (Fig. S11A–S11H). Meanwhile, the abundance of IFN-γ^{+} CD8^{+} T cells in the tumors was evaluated by flow cytometry (Supporting Information Fig. S12A and S12B). After the treatment with the *in situ* nano-vaccines, the percentage of IFN-γ^{+} CD8^{+} T cells in

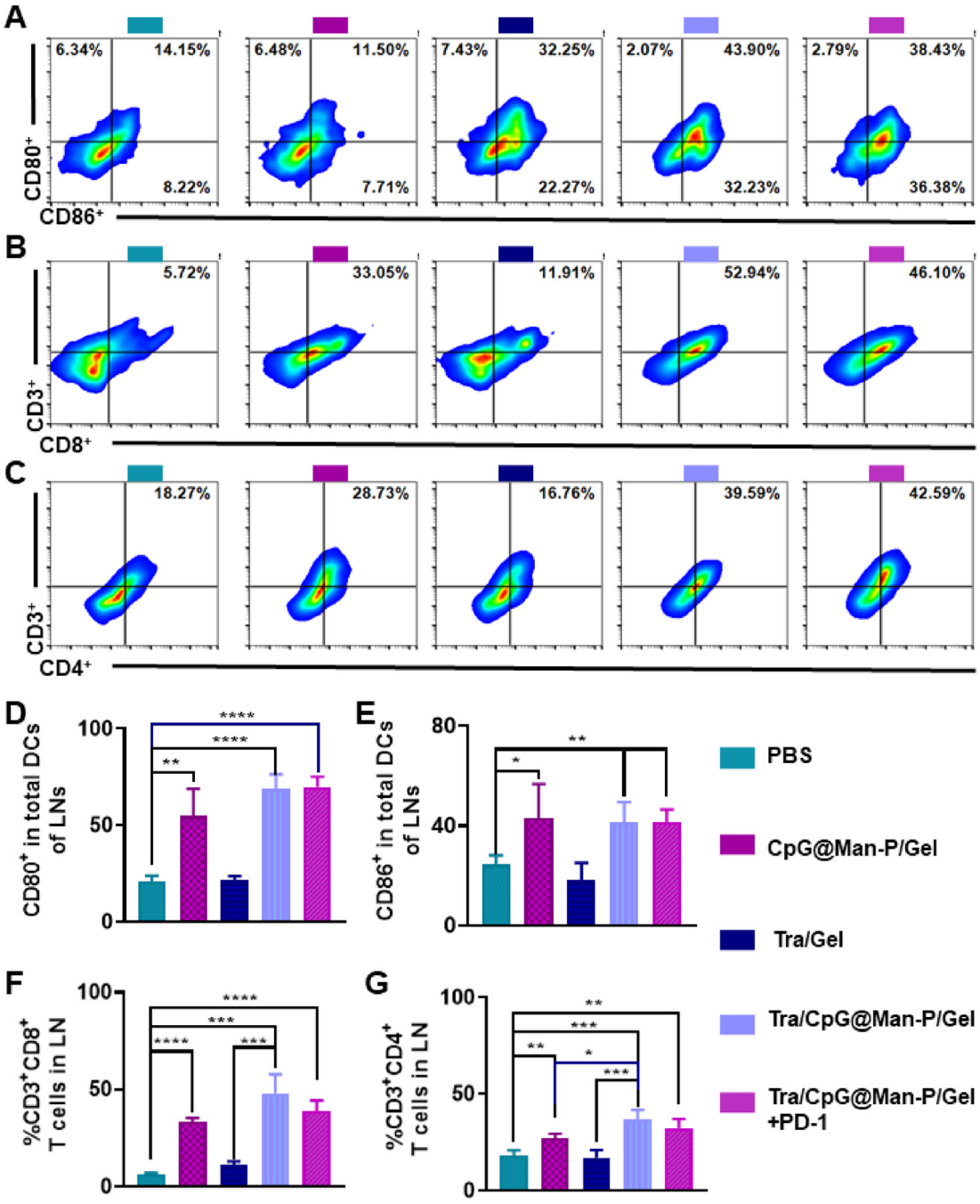

Figure 4 Immune response in LNs. Abundant of $CD80^+$ $CD86^+$ (A) cells gated on $CD11c^+$ cells in the LNs, indicating the maturation of DCs. Percentages of $CD3^+$ $CD8^+$ cells (B) and $CD3^+$ $CD4^+$ cells (C) in LNs, suggesting the T cell infiltration. Quantification of $CD80^+$ DCs (D), $CD86^+$ DCs (E), $CD8^+$ T cells (F), and $CD4^+$ T cells (G) in the LNs after treatment with different formulations. Error bars represent mean ± SD ($n = 3-4$). Statistical significance was set at $^*P < 0.05$, $^{**}P < 0.01$, $^{***}P < 0.001$, $^{****}P < 0.0001$, and ns, not significant.

the tumor was increased heavily, compared to the PBS and Tra/Gel groups. These results jointly demonstrated that the *in situ* nano-vaccines can inhibit the development of primary and distant tumors and induce potent antitumor immune responses.

3.6. *Evaluation of anti-metastasis effect*

Anti-metastasis effect was evaluated using an ID8 intraperitoneal injection model (Fig. 7A). After the last administration, the mice were fed for another two weeks to allow the development of multiple types of metastases. The metastatic tumors in the gastrointestinal tract, uterine, and lung tissues were observed (Fig. 7B–G). The images and quantitative results of gastrointestinal tract metastasis showed the superiority of Tra/CpG@Man-P/Gel and Tra/CpG@Man-P/Gel + PD-1 in inhibiting the metastatic tumors in the abdominal cavity (Fig. 7B and E). The number of metastatic tumors in the abdominal cavity was reduced by 14.2- and 7.2-fold in Tra/CpG@Man-P/Gel group compared to PBS and

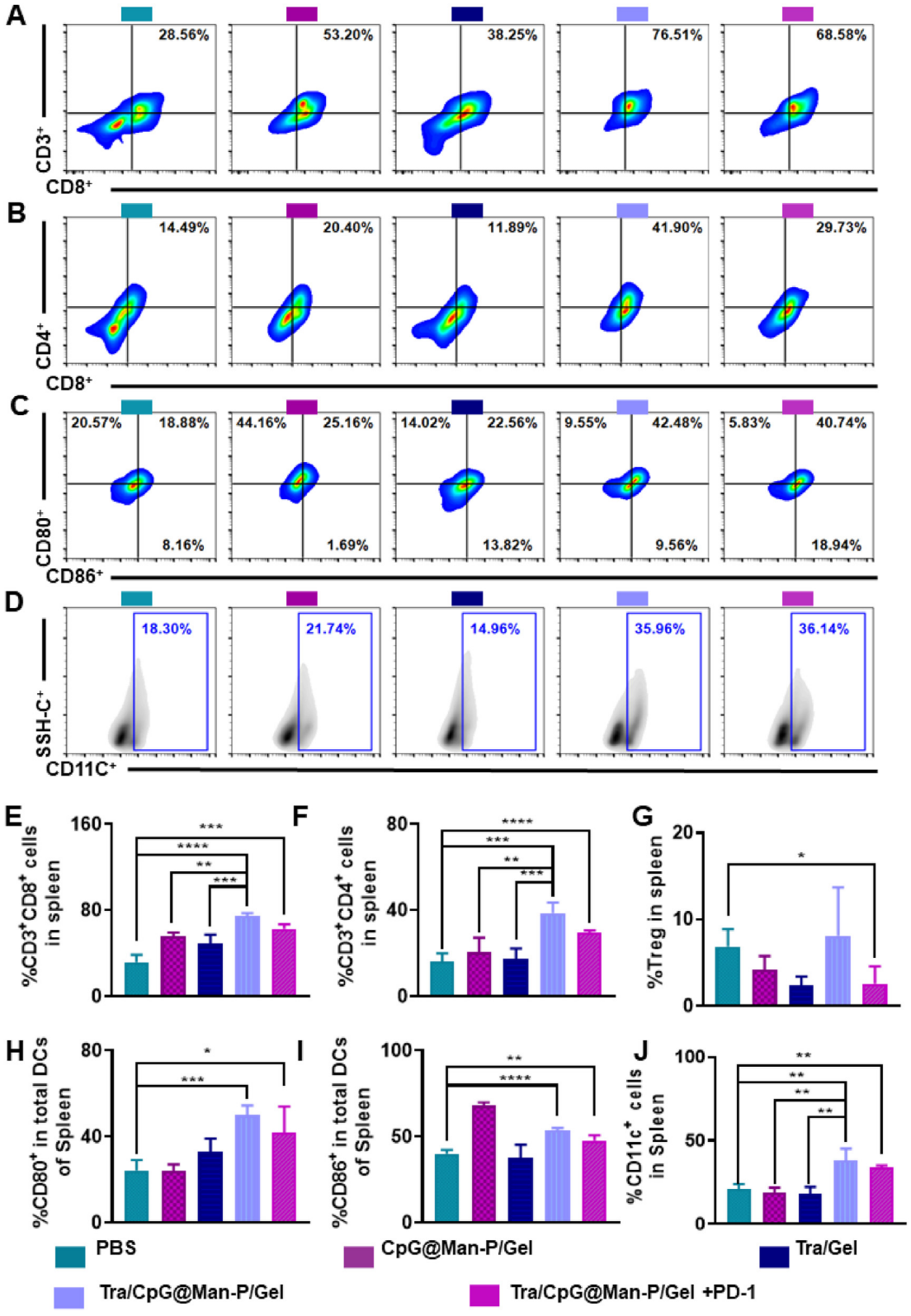

Figure 5 Antitumor immunity in spleens. Percentages of $CD8^+$ T cells (A) and $CD4^+$ T cells (B) in spleens detected by flow cytometry. Abundant of $CD80^+$ DCs (C) and $CD86^+$ DCs (D) in spleens. Percentages of $CD8^+$ T cells (E), $CD4^+$ T cells (F), and T_{reg} cells (G) in spleens gated by $CD3^+$ cells. Quantification of $CD80^+$ DCs (H), $CD86^+$ DCs (I), and $CD11c^+$ cells (J) in the spleens after treatment with different formulations. Error bars represent mean ± SD ($n = 3–4$). Statistical significance was set at $^*P < 0.05$, $^{**}P < 0.01$, $^{***}P < 0.001$, and ns, not significant.

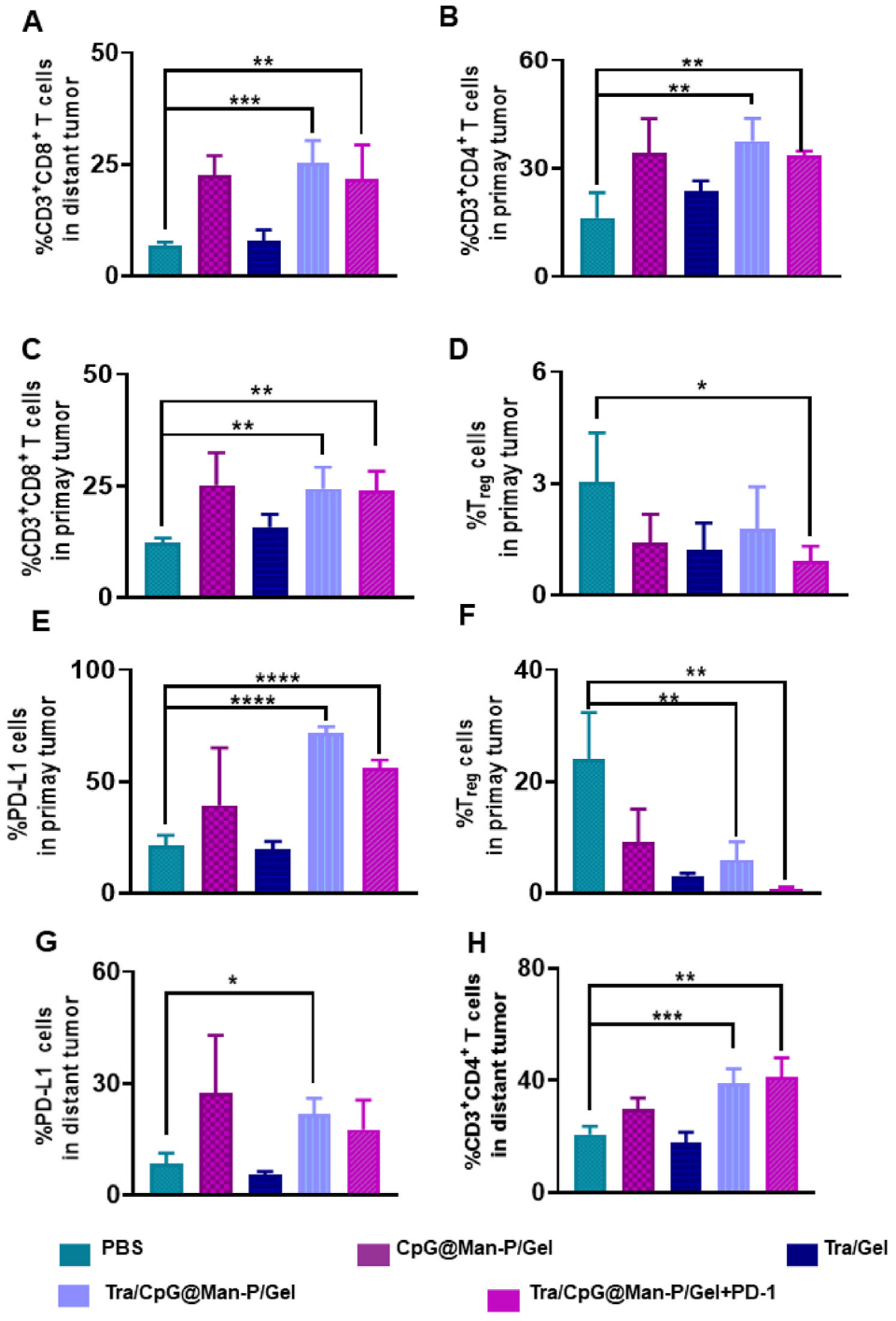

Figure 6 Immune response in primary and distant tumors. (A−D) Percentages of $CD8^+$ T cells (A), $CD4^+$ T cells (B), PD-$L1^+$ cells (C), and T_{reg} cells (D) in primary tumors after treatment with different formulations. (E−H) Percentages of $CD8^+$ T cells (E), $CD4^+$ T cells (F), PD-$L1^+$ cells (G), and T_{reg} cells (H) in distant tumors after treatment with different formulations. Error bars represent mean ± SD (n = 3−4). Statistical significance was set at $^*P < 0.05$, $^{**}P < 0.01$, $^{***}P < 0.001$, $^{****}P < 0.0001$, and ns, not significant.

Tra/Gel groups, respectively. Similarly, there were fewer metastatic tumors attached to the uterine, according to the images and weights of uterine appendages (Fig. 7C and F). The PBS group exhibited the strongest uterine metastasis and the uterine appendages in the PBS group were around 3.1- and 3.3-fold heavier than that in Tra/CpG@Man-P/Gel and Tra/CpG@Man-P/Gel + PD-1 groups, respectively. Meanwhile, the lung metastases were heavily inhibited by CpG@Man-P/Gel, Tra/CpG@Man-P/Gel, and Tra/CpG@Man-P/Gel + PD-1 treatments (Fig. 7D and G). Moreover, the HE images of lung tissues also showed that there were obvious lung metastatic tumors in the PBS group, which were suppressed heavily by Tra/CpG@Man-P/Gel, and Tra/

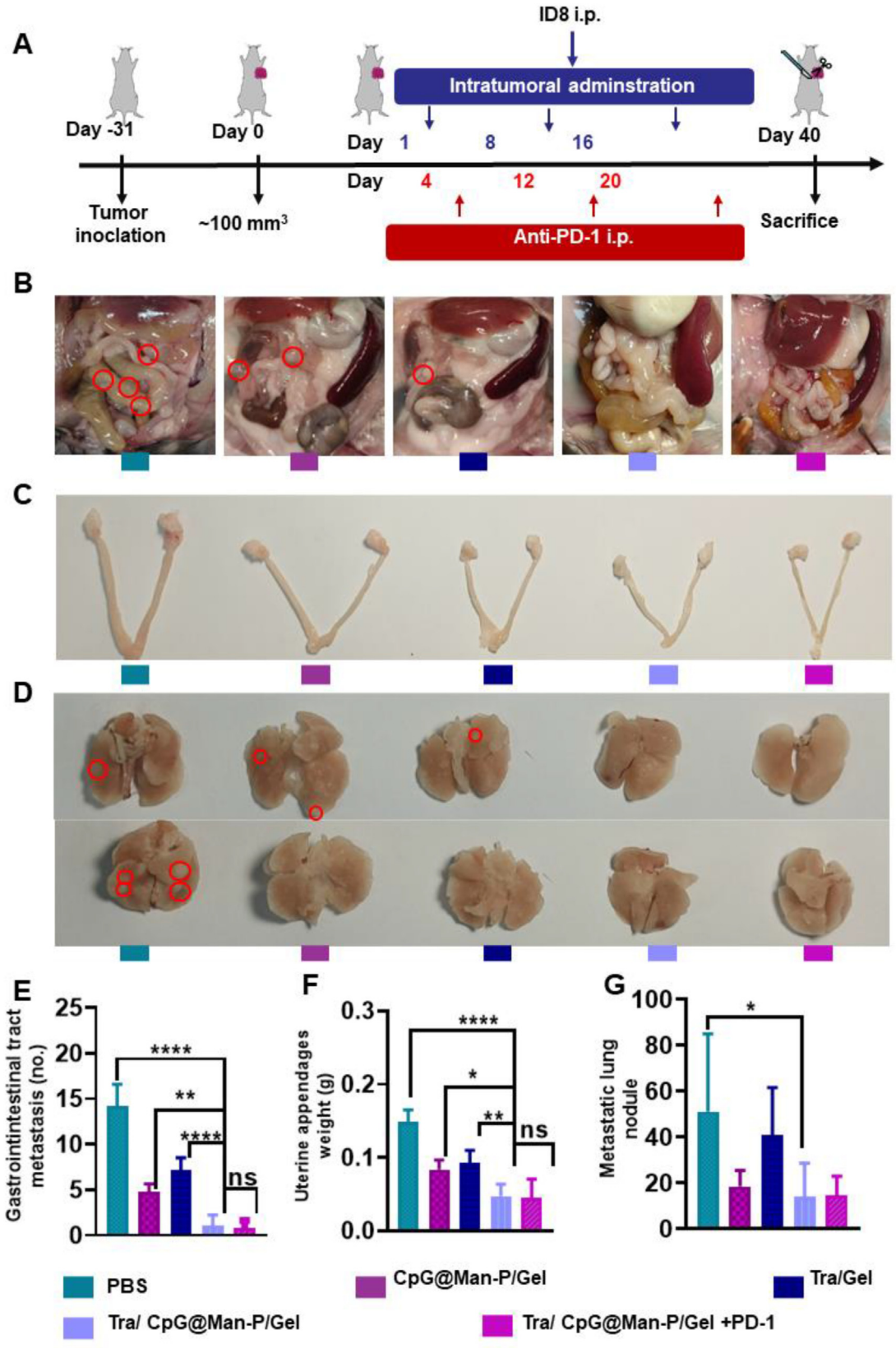

Figure 7 Anti-metastasis effect of nano-adjuvants. (A) Schematic depicting the experimental approach. (B, C) Images of the abdomen (B), uterine (C), and lung tissues (D) after treatment. Quantitative results of gastrointestinal tract metastasis (E), uterine appendage weights (F), and lung metastasis nodes (G) after treatment with different formulations. Error bars represent mean ± SD ($n = 4$). Statistical significance was set at $^{*}P < 0.05$, $^{**}P < 0.01$, $^{***}P < 0.001$, and ns, not significant.

CpG@Man-P/Gel + PD-1 treatments (Fig. S12C). These results jointly demonstrated that Tra/CpG@Man-P/Gel had great inhibitory on metastases of ovarian cancer, equipped with an improved LDIMP process, and had great potential for cancer immunotherapy.

4. Conclusions

In conclusion, we successfully constructed *in situ* nano-vaccines Tra/CpG@Man-P/Gel consisting of Tra, nano-adjuvants CpG@Man-P with different particle sizes, and nanogels formed by cross-linking of 4-arm-PEG-Mal with MMP-2-responsive peptides. The hydrogel responded to the highly expressed MMP-2 in the tumor microenvironment by sustained release of Tra and the nano-adjuvant CpG@Man-P. The former induces immunogenic death of tumor cells and generates whole-cell tumor antigens, resulting in a proto-antigenic library that can be continuously adsorbed by the nano-adjuvant to form a nano-vaccine. Thanks to the Man modification, the nano-vaccine can be delivered to LNs and endocytosed by DCs, and the maturation of DCs is promoted by the co-delivery of adjuvant and antigen, which further enhances the activation and proliferation of T cells, and ultimately activates a strong and effective anti-tumor immune response. *In vitro* and *in vivo* experiments showed that CpG@Man-P with 40 nm size could be released from the nanogels faster and drained more to the LNs, inducing maturation of DCs and T cell activation. Thus, we finally chose a nano-adjuvant with a 40 nm size to construct *in situ* tumor vaccines for the treatment of ovarian cancer and its metastasis. Combined with PD-1 blockade, the *in situ* nano-vaccines showed potent anti-tumor effects: significant inhibition of *in situ* and distal tumor growth, elevated proportion of mature DCs in LNs and spleen, increased T-cell infiltration, decreased Treg cells, and significant reduction of metastasis. All these results demonstrated that the *in situ* tumor vaccine (in combination with ICB) remodeled the tumor immunosuppressive microenvironment, and generated a potent anti-tumor immune response, suppressing primary and metastatic tumors. Therefore, *in situ* tumor nano-vaccines had great superiority to traditional immunotherapy, showing great prospects in cancer therapy.

Acknowledgments

The work was supported by the National Natural Science Foundation of China (No. 82102769), the 111 Project (No. B18035, China), the Fundamental of Research Funds for the Central Universities and Beijing Natural Science Foundation (No. L212054, China).

Author contributions

Yuan Li: Conceptualization, Investigation, Methodology, Writing − review & editing. Fan Tong: Conceptualization, Investigation, Methodology, Writing − original draft. Yufan Wang: Investigation, Methodology. Jing Wang: Software, Writing − review & editing. Manqi Wu: Investigation and Methodology. Hanmei Li: Methodology and Software. Hongyan Guo: Funding acquisition, Supervision. Huile Gao: Conceptualization, Supervision, Funding acquisition.

Conflicts of interest

There are no conflicts to declare.

Appendix A. Supporting information

Supporting information to this article can be found online at https://doi.org/10.1016/j.apsb.2024.06.003.

References

1. Cheng S, Xu C, Jin Y, Li Y, Zhong C, Ma J, et al. Artificial mini dendritic cells boost t cell−based immunotherapy for ovarian cancer. *Adv Sci* 2020;**7**:1903301.
2. Ledermann JA. Front-line therapy of advanced ovarian cancer: new approaches. *Ann Oncol* 2017;**28**:viii46−50.
3. Morse CB, Voillet V, Bates BM, Chiu EY, Garcia NM, Gottardo R, et al. Development of a clinically relevant ovarian cancer model incorporating surgical cytoreduction to evaluate treatment of micrometastatic disease. *Gynecol Oncol* 2021;**160**:427−37.
4. Cress RD, Chen YS, Morris CR, Petersen M, Leiserowitz GS. Characteristics of long-term survivors of epithelial ovarian cancer. *Obstet Gynecol* 2015;**126**:491−7.
5. Zhang J, Guo Y, Pan G, Wang P, Li Y, Zhu X, et al. Injectable drug-conjugated DNA hydrogel for local chemotherapy to prevent tumor recurrence. *ACS Appl Mater Inter* 2020;**12**:21441−9.
6. Kaplan JA, Liu R, Freedman JD, Padera R, Schwartz J, Colson YL, et al. Prevention of lung cancer recurrence using cisplatin-loaded superhydrophobic nanofiber meshes. *Biomaterials* 2016;**76**:273−81.
7. Matsuo K, Eno ML, Im DD, Rosenshein NB, Sood AK. Clinical relevance of extent of extreme drug resistance in epithelial ovarian carcinoma. *Gynecol Oncol* 2010;**116**:61−5.
8. Sun C, Li X, Guo E, Li N, Zhou B, Lu H, et al. MCP-1/CCR-2 axis in adipocytes and cancer cell respectively facilitates ovarian cancer peritoneal metastasis. *Oncogene* 2020;**39**:1681−95.
9. Wang T, Wang D, Yu H, Feng B, Zhou F, Zhang H, et al. A cancer vaccine-mediated postoperative immunotherapy for recurrent and metastatic tumors. *Nat Commun* 2018;**9**:1532.
10. Whiteside TL, Demaria S, Rodriguez-Ruiz ME, Zarour HM, Melero I. Emerging opportunities and challenges in cancer immunotherapy. *Clin Cancer Res* 2016;**22**:1845−55.
11. Li Q, Shi Z, Zhang F, Zeng W, Zhu D, Mei L. Symphony of nanomaterials and immunotherapy based on the cancer−immunity cycle. *Acta Pharm Sin B* 2022;**12**:107−34.
12. Zhang F, Lu G, Wen X, Li F, Ji X, Li Q, et al. Magnetic nanoparticles coated with polyphenols for spatio-temporally controlled cancer photothermal/immunotherapy. *J Control Release* 2020;**326**:131−9.
13. Zhang H, Zhang Y, Hu H, Yang W, Xia X, Lei L, et al. *In situ* tumor vaccine for lymph nodes delivery and cancer therapy based on small size nanoadjuvant. *Small* 2023;**19**:2301041.
14. Yi Y, Yu M, Li W, Zhu D, Mei L, Ou M. Vaccine-like nanomedicine for cancer immunotherapy. *J Control Release* 2023;**355**:760−78.
15. Du G, Qin M, Sun X. Recent progress in application of nanovaccines for enhancing mucosal immune responses. *Acta Pharm Sin B* 2023;**13**:2334−45.
16. Qin L, Cao J, Shao K, Tong F, Yang Z, Lei T, et al. A tumor-to-lymph procedure navigated versatile gel system for combinatorial therapy against tumor recurrence and metastasis. *Sci Adv* 2020;**6**:eabb3116.
17. Saxena M, van der Burg SH, Melief CJM, Bhardwaj N. Therapeutic cancer vaccines. *Nat Rev Cancer* 2021;**21**:360−78.
18. Gong S, Liang X, Zhang M, Li L, He T, Yuan Y, et al. Tumor microenvironment-activated hydrogel platform with programmed release property evokes a cascade-amplified immune response against tumor growth, metastasis and recurrence. *Small* 2022;**18**:2107061.
19. Xu Y, Xiong J, Sun X, Gao H. Targeted nanomedicines remodeling immunosuppressive tumor microenvironment for enhanced cancer immunotherapy. *Acta Pharm Sin B* 2022;**12**:4327−47.
20. Diao L, Liu M. Rethinking antigen source: cancer vaccines based on whole tumor cell/tissue lysate or whole tumor cell. *Adv Sci* 2023;**10**:2300121.

21. Xu J, Lv J, Zhuang Q, Yang Z, Cao Z, Xu L, et al. A general strategy towards personalized nanovaccines based on fluoropolymers for post-surgical cancer immunotherapy. *Nat Nanotechnol* 2020;**15**:1043−52.
22. Scheetz L, Park KS, Li Q, Lowenstein PR, Castro MG, Schwendeman A, et al. Engineering patient-specific cancer immunotherapies. *Nat Biomed Eng* 2019;**3**:768−82.
23. Shetty K, Ott PA. Personal neoantigen vaccines for the treatment of cancer. *Annu Rev Cancer Biol* 2021;**5**:259−76.
24. Yu X, Dai Y, Zhao Y, Qi S, Liu L, Lu L, et al. Melittin-lipid nanoparticles target to lymph nodes and elicit a systemic anti-tumor immune response. *Nat Commun* 2020;**11**:1110.
25. Xiong X, Zhao J, Pan J, Liu C, Guo X, Zhou S. Personalized nanovaccine coated with calcinetin-expressed cancer cell membrane antigen for cancer immunotherapy. *Nano Lett* 2021;**21**:8418−25.
26. Chen J, Qiu M, Ye Z, Nyalile T, Li Y, Glass Z, et al. *In situ* cancer vaccination using lipidoid nanoparticles. *Sci Adv* 2022;**7**:eabf1244.
27. Zhang M, Jin X, Gao M, Zhang Y, Tang BZ. A self-reporting fluorescent salicylaldehyde−chlorambucil conjugate as a type-ii ICD inducer for cancer vaccines. *Adv Mater* 2022;**34**:2205701.
28. Jin L, Yang D, Song Y, Li D, Xu W, Zhu Y, et al. *In situ* programming of nanovaccines for lymph node-targeted delivery and cancer immunotherapy. *ACS Nano* 2022;**16**:15226−36.
29. Sun M, Liu Z, Wu L, Yang J, Ren J, Qu X. Bioorthogonal-activated *in situ* vaccine mediated by a COF-based catalytic platform for potent cancer immunotherapy. *J Am Chem Soc* 2023;**145**:5330−41.
30. Liu X, Liu Y, Li X, Huang J, Guo X, Zhang J, et al. ER-targeting PDT converts tumors into *in situ* therapeutic tumor vaccines. *ACS Nano* 2022;**16**:9240−53.
31. Lian T, Li C, Wang H. Trametinib in the treatment of multiple malignancies harboring mek1 mutations. *Cancer Treat Rev* 2019;**81**:101907.
32. Wang D, Cong J, Fu B, Zheng X, Sun R, Tian Z, et al. Immunogenic chemotherapy effectively inhibits kras-driven lung cancer. *Cancer Lett* 2020;**492**:31−43.
33. Wabitsch S, Tandon M, Ruf B, Zhang Q, McCallen JD, McVey JC, et al. Anti-PD-1 in combination with trametinib suppresses tumor growth and improves survival of intrahepatic cholangiocarcinoma in mice. *Cell Mol Gastroenterol Hepatol* 2021;**12**:1166−78.
34. Topalian SL, Drake CG, Pardoll DM. Targeting the PD-1/B7-H1(PD-L1) pathway to activate anti-tumor immunity. *Curr Opin Immunol* 2012;**24**:207−12.
35. Irvine DJ, Dane EL. Enhancing cancer immunotherapy with nanomedicine. *Nat Rev Immunol* 2020;**20**:321−34.
36. Jiang H, Wang Q, Sun X. Lymph node targeting strategies to improve vaccination efficacy. *J Control Release* 2017;**267**:47−56.
37. Xu Y, Ma S, Zhao J, Chen H, Si X, Huang Z, et al. Mannan-decorated pathogen-like polymeric nanoparticles as nanovaccine carriers for eliciting superior anticancer immunity. *Biomaterials* 2022;**284**:121489.
38. Song W, Das M, Xu Y, Si X, Zhang Y, Tang Z, et al. Leveraging biomaterials for cancer immunotherapy: targeting pattern recognition receptors. *Mater Today Nano* 2019;**5**:100029.
39. Żelechowska P, Brzezińska-Błaszczyk E, Różalska S, Agier J, Kozłowska E. Mannan activates tissue native and IGE-sensitized mast cells to proinflammatory response and chemotaxis in TLR4-dependent manner. *J Leukoc Biol* 2021;**109**:931−42.
40. Zhang Y, Jiang M, Du G, Zhong X, He C, Qin M, et al. An antigen self-assembled and dendritic cell-targeted nanovaccine for enhanced immunity against cancer. *Acta Pharm Sin B* 2023;**13**:3518−34.
41. Bachmann MF, Jennings GT. Vaccine delivery: a matter of size, geometry, kinetics and molecular patterns. *Nat Rev Immunol* 2010;**10**:787−96.
42. Liang X, Li L, Li X, He T, Gong S, Zhu S, et al. A spontaneous multifunctional hydrogel vaccine amplifies the innate immune response to launch a powerful antitumor adaptive immune response. *Theranostics* 2021;**11**:6936−49.
43. Huang L, Li Y, Du Y, Zhang Y, Wang X, Ding Y, et al. Mild photothermal therapy potentiates anti-PD-L1 treatment for immunologically cold tumors *via* an all-in-one and all-in-control strategy. *Nat Commun* 2019;**10**:4871.
44. Yan J, Zhang Z, Zhan X, Chen K, Pu Y, Liang Y, et al. *In situ* injection of dual-delivery peg based MMP-2 sensitive hydrogels for enhanced tumor penetration and chemo-immune combination therapy. *Nanoscale* 2021;**13**:9577−89.
45. Zhang C, Ma J, Wang Q, Wang Y, Kang Z, Chen Y, et al. pH/thermal dual-sensitive nanoparticle-hydrogel composite based on pluronic and carboxymethyl chitosan for *in situ* injection and enhanced chemo-photothermal antitumor effect. *ACS Appl Nano Mater* 2023;**6**:7841−54.
46. Lindsey ML. Assigning matrix metalloproteinase roles in ischaemic cardiac remodelling. *Nat Rev Cardiol* 2018;**15**:471−9.
47. Liu R, Luo C, Pang Z, Zhang J, Ruan S, Wu M, et al. Advances of nanoparticles as drug delivery systems for disease diagnosis and treatment. *Chin Chem Lett* 2023;**34**:107518.
48. Yu J, Chen F, Wang X, Dong N, Lu C, Yang G, et al. Synthesis and characterization of mmp degradable and maleimide cross-linked peg hydrogels for tissue engineering scaffolds. *Polym Degrad Stab* 2016;**133**:312−20.